


RESEARCH

Open Access



# Conducting molybdenum sulfide/graphene oxide/polyvinyl alcohol nanocomposite hydrogel for repairing spinal cord injury

Lingling Chen<sup>1†</sup>, Wanshun Wang<sup>1,2†</sup>, Zefeng Lin<sup>1</sup>, Yao Lu<sup>3,4</sup>, Hu Chen<sup>1,3</sup>, Binglin Li<sup>1</sup>, Zhan Li<sup>1</sup>, Hong Xia<sup>1,3\*</sup>, Lihua Li<sup>5\*</sup>  and Tao Zhang<sup>1,3\*</sup>

## Abstract

A sort of composite hydrogel with good biocompatibility, suppleness, high conductivity, and anti-inflammatory activity based on polyvinyl alcohol (PVA) and molybdenum sulfide/graphene oxide (MoS<sub>2</sub>/GO) nanomaterial has been developed for spinal cord injury (SCI) restoration. The developed (MoS<sub>2</sub>/GO/PVA) hydrogel exhibits excellent mechanical properties, outstanding electronic conductivity, and inflammation attenuation activity. It can promote neural stem cells into neurons differentiation as well as inhibit the astrocytes development in vitro. In addition, the composite hydrogel shows a high anti-inflammatory effect. After implantation of the composite hydrogel in mice, it could activate the endogenous regeneration of the spinal cord and inhibit the activation of glial cells in the injured area, thus resulting in the recovery of locomotor function. Overall, our work provides a new sort of hydrogels for SCI reparation, which shows great promise for improving the dilemma in SCI therapy.

**Keywords:** Spinal cord injury, Molybdenum sulfide/oxidized graphene, Hydrogel, Conductive and mechanical adaptation, Spinal cord reparation, Anti-inflammation

\*Correspondence: gzxiahong2@126.com; lihua361@126.com; gzlupus@126.com

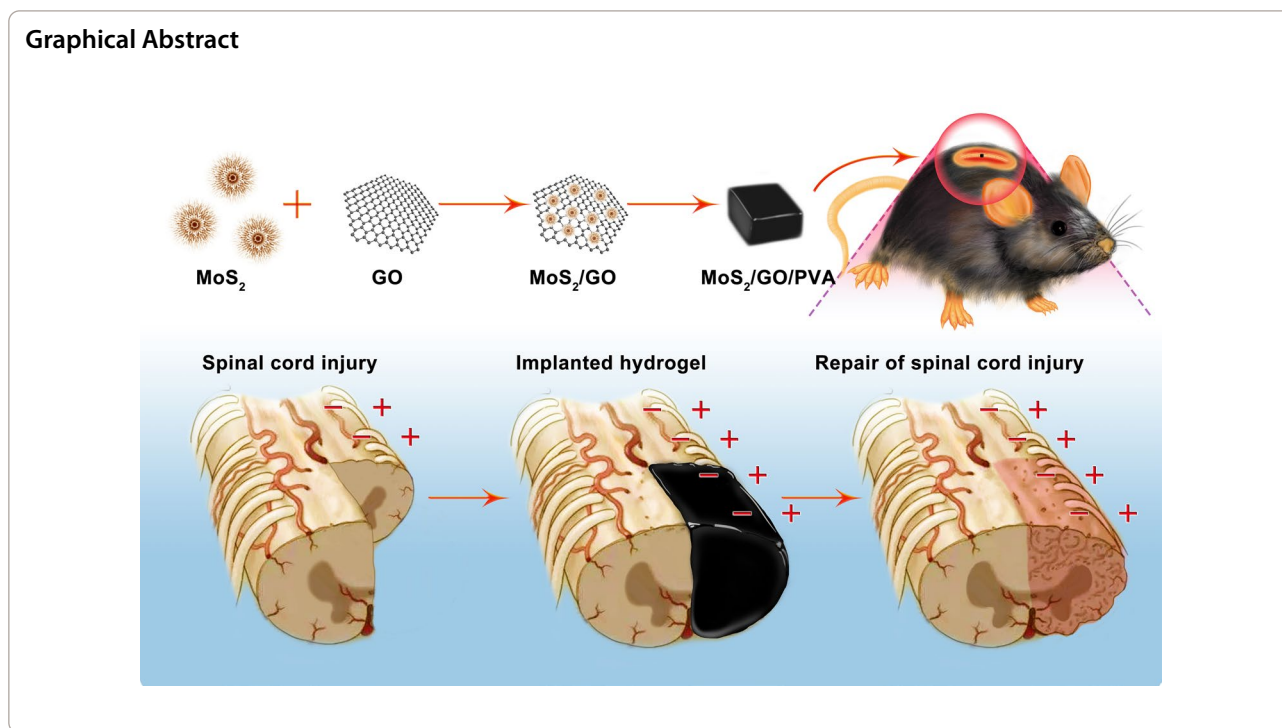
†Lingling Chen and Wanshun Wang contributed equally to this work

<sup>1</sup> Guangdong Key Lab of Orthopedic Technology and Implant Materials, Key Laboratory of Trauma & Tissue Repair of Tropical Area of PLA, Orthopedic Center, General Hospital of Southern Theater Command of PLA, Guangzhou 510010, Guangdong, China

<sup>5</sup> Department of Applied Physics, The Hong Kong Polytechnic University, Kowloon 999077, Hong Kong, China

Full list of author information is available at the end of the article





## Introduction

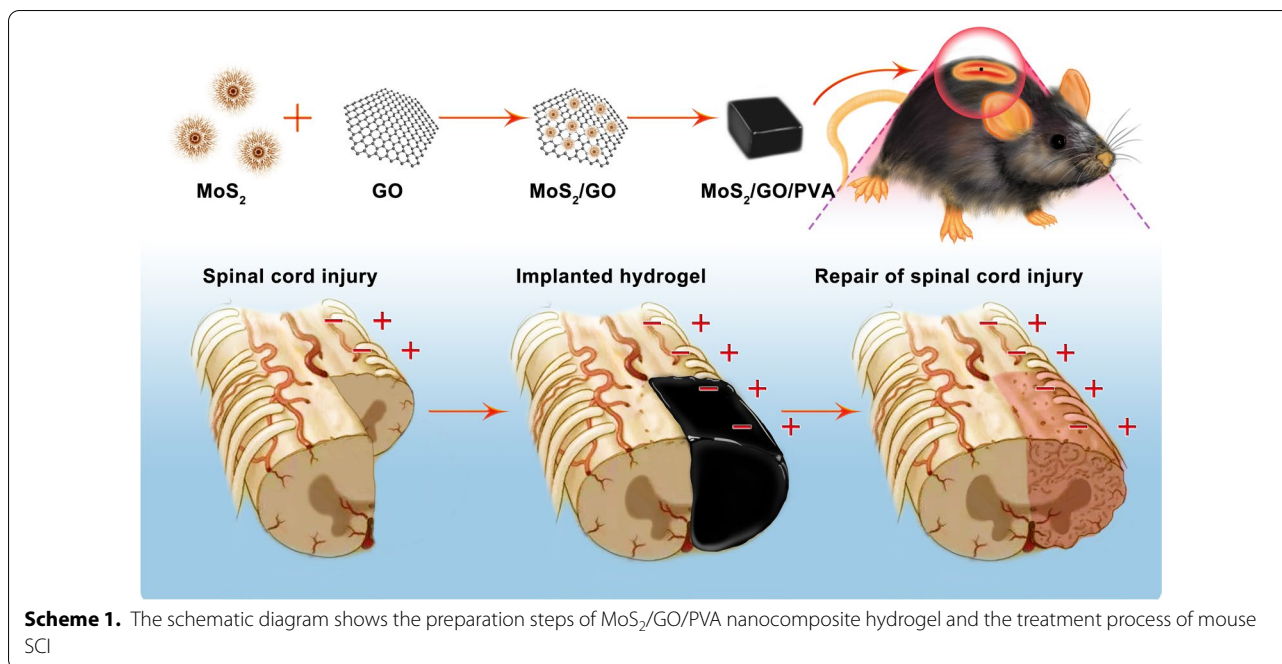
Spinal cord injury (SCI), as a destructive central nervous system (CNS) trauma, is an intractable medical challenge, which could lead to motor dysfunction and paralysis for a lifetime [1]. According to the World Health Organization (WHO), about 250,000–500,000 people suffer from SCI each year worldwide [2]. And the global burden of SCI is gradually increasing because of traffic accidents [3]. Although enormous efforts have been made for SCI treatment during the past years, there is still a lack of effective treatment for SCI recovery due to the rigid microenvironment and limited regeneration ability of the central nervous system [4]. Engineering implants with high biological activity and conductivity open new avenues for improving SCI recovery.

Bioactive materials with conductive properties can mediate the signal transduction between cells and promote trauma recovery. In recent years, two-dimension (2D) nanomaterials, including graphite oxide (GO) and molybdenum sulfide (MoS<sub>2</sub>), have attracted much attention as new bioactive materials. GO has been used for the study of SCI because of its unique physical and chemical properties, including large loading volume, hydrophilic functional groups, and excellent biocompatibility [5]. Recent studies have also shown that GO not only facilitated the differentiation of neural stem cells (NE-4C) to neuron cells, but also promoted the directional growth of neuronal axons during the repair of SCI [6, 7]. Notably, the primary injury in SCI damages cells and initiates

a complex secondary injury cascade local hemorrhage, edema, ischemia, internal environment disorders, excessive reactive oxygen species (ROS) production, and the inflammatory factors, which will further lead to nerve cell damage [8] and destroy the connection of neurons [9].

MoS<sub>2</sub>, with high electrical conductivity and catalytic activity, is preferred as doped materials [10]. Previous studies suggested that MoS<sub>2</sub> promoted anti-inflammatory, macrophage-modulating SCI immunotherapy and provided neuro-reconnection and protection, resulting in locomotor recovery correspondingly [11]. Hence, MoS<sub>2</sub>/GO displays great potential for SCI repair. More importantly, materials for renovation should have high elasticity to eliminate the mechanical stress on the spinal cord and low friction coefficient [12, 13].

To address the dilemma in SCI therapy, we proposed polyvinyl alcohol PVA hydrogels with MoS<sub>2</sub>/GO nanosheets (NSs). PVA is a promising candidate because it can prevent the migration of inflammatory cells and reduce secondary injury after SCI. The synthesized composite hydrogel exhibits good suppleness, proper Young's modulus, and high electrical conductivity. They promoted the directional differentiation of neural stem cells into neuron cells and scavenged reactive oxygen species (ROS) in the injured part. In addition, the composite hydrogel can inhibit the differentiation of M1 and activate M2 macrophage, thus resulting in the improvement of inflammatory cytokines (Scheme 1). More importantly, MoS<sub>2</sub>/GO/PVA composite hydrogels could remarkably



promote spinal cord tissue repair and locomotor recovery in vivo. Therefore, MoS<sub>2</sub>/GO/PVA composite hydrogel works as an excellent biomaterial for the treatment of SCI and has a promising clinical application prospect.

## Materials and methods

### Composite hydrogel synthesis

Firstly, GO NSs were prepared from graphite powder. A large beaker was placed on ice, 110 mL of H<sub>2</sub>SO<sub>4</sub> (98%) was added, then 5 g graphite was added at 4 °C, and 2.5 g NaNO<sub>3</sub> and 15 g KMnO<sub>4</sub> were slowly added in order, and the solution was purple green after 90 min of stirring on a magnetic stirrer. The ice was removed, and the mixture was reacted for another 30 min. The solution was slowly added to 220 mL ddH<sub>2</sub>O and heated to 70 °C, then 20 mL H<sub>2</sub>O<sub>2</sub> (5%) was slowly added to the solution. At this time, the solution turned golden. After the reaction, the sample was centrifuged and washed for several times to remove the overabundant acid. The sample was dried at 80 °C, and the GO NSs were obtained after grinding.

Synthesis of MoS<sub>2</sub> and MoS<sub>2</sub>/GO NSs, 0.6 g sodium molybdate was dissolved in 70 mL ddH<sub>2</sub>O, 0.78 g thio-urea and 0.1 g polyvinyl pyrrolidone (PVP) were added to the solution, after ultrasonicated for 20 min, the solution was transferred into a 100 mL Teflon-lined autoclave, sealed, and heated up to 240 °C for 24 h in an electric furnace. After the reaction naturally fell to room temperature, the precipitates were got from centrifugation at 8000 rpm for 10 min and then washed with ethanol

and distilled water to remove the impurities. Similarly, the MoS<sub>2</sub>/GO NSs were synthesized with the abovementioned methods after replacing the PVP with GO. Additionally, all the MoS<sub>2</sub> NSs were closely attached on the GO NSs during the hydrothermal process.

Synthesis of GO/PVA, MoS<sub>2</sub>/PVA, and MoS<sub>2</sub>/GO/PVA composite hydrogel. The PVA concentration was set to 2.5%, 5%, 7.5%, 10%, 12.5%, and 15% (w/v), respectively. After repeatedly freezing and thawing overnight at −20 °C, composite hydrogels with different properties were obtained. The preparation of GO/PVA, MoS<sub>2</sub>/PVA, and MoS<sub>2</sub>/GO/PVA composite hydrogel were as below, 100 mL MoS<sub>2</sub>, GO and MoS<sub>2</sub>/GO solutions (125 μg/mL) were mixed with 100 mL PVA (2 g/mL), respectively, and the different solutions were repeatedly freezing and thawing overnight at −20 °C to get 62.5 μg/mL GO/PVA, MoS<sub>2</sub>/PVA, and MoS<sub>2</sub>/GO/PVA composite hydrogel.

### Characterization

The morphology of the nanomaterials was observed by high-resolution transmission electron microscopy (HRTEM, JEOL 2100, Japan) after MoS<sub>2</sub>, GO, and MoS<sub>2</sub>/GO NSs suspensions were placed on a carbon-coated copper net. The surface morphology of the hydrogel was observed using a scanning electron microscope (Nova Nano SEM 430, FEI). Raman spectra of MoS<sub>2</sub>, GO, and MoS<sub>2</sub>/GO NSs were recorded using a confocal Raman microscope (Labram HR, Horiba Jobin Yvon, France). The X-ray diffraction (XRD) patterns of MoS<sub>2</sub>/GO and

MoS<sub>2</sub> were obtained using the Siemens Kristalloflex 810 D-500 X-ray diffractometer (Karlsruhe, Germany) in the 2θ range of 5° to 90° at 40 kV and 30 mA, λ = 1.5406 Å radiation. Fourier transform infrared (FTIR) spectra were measured on a PerkinElmer 580B IR spectrophotometer using the KBr pellet technique. The high-angle annular dark-field scanning TEM (HAADF-STEM) image and element mapping were obtained from the electron microscope (Hitachi 2100, Japan) with an accelerating voltage of 210 kV. The x-ray photoelectron spectroscopy (XPS) spectra was applied to determine the element type and chemical valence state of the MoS<sub>2</sub>/GO NSs using the electron spectrometer (ESCALAB 250Xi, Thermo Scientific, USA). The Zeta potential of MoS<sub>2</sub>, GO, and MoS<sub>2</sub>/GO NSs were measured by Zetasizer Nano Z (Malvern, UK).

#### Peroxidase-like activity

Peroxidase (POD)-like activity of GO, MoS<sub>2</sub>, and MoS<sub>2</sub>/GO NSs was evaluated using 3,3',5,5'-tetramethylbenzidine (TMB, Macklin, China) according to our previous reports [14]. For the oxidation of TMB by H<sub>2</sub>O<sub>2</sub>, three groups with various reagents combinations were set as followed: (1) TMB + H<sub>2</sub>O<sub>2</sub>, (2) TMB + GO or MoS<sub>2</sub> or MoS<sub>2</sub>/GO NSs, (3) TMB + H<sub>2</sub>O<sub>2</sub> + GO or MoS<sub>2</sub> or MoS<sub>2</sub>/GO NSs. 100 μL of GO or MoS<sub>2</sub> or MoS<sub>2</sub>/GO NSs (100 μg/mL) were suspended in acetic acid-sodium acetate buffer (0.2 M:0.2 M, pH = 4.6), respectively. Then, 100 μL of TMB solution in dimethyl sulfoxide (2 mM) as substrate, or 100 μL of H<sub>2</sub>O<sub>2</sub> (10 mM) were added. During half-hour incubation at room temperature, changes in the UV-Vis absorption spectra were monitored using the UV-Vis spectrometer every 5 mins.

#### Conductivity

The conductivity of hydrogels was detected by a digital multimeter (fluke 8845A, American), the cross-section and length of hydrogels were measured by digital vernier caliper (Neiko 01407A, American) (Additional file 1: Fig. S6), and the conductivity of hydrogel was calculated comprehensively.

#### Swelling ratio

To evaluate the swelling ability of nanocomposite hydrogels, the weight of the dried hydrogels and wet hydrogels after being immersed in 37 °C phosphate buffer saline (PBS) for 24 h were recorded, respectively. The swelling rate was determined by using the following equation:

$$\text{Swelling rate (\%)} = \frac{\text{Wet weight} - \text{Dry weight}}{\text{Dry weight}} \times 100 \quad (1)$$

#### Biodegradation

Simulated body fluid (SBF) was used to detect the biodegradation of nanohydrogels. After the initial weight were weighed, the nanohydrogels with a volume of about 0.5 cm<sup>3</sup> were immersed in 10 mL SBF and placed in 15 ml centrifuge tubes, and stirred at a constant speed of 100 rpm in 37 °C. 10% PVA hydrogel was used as Control group. SBF was replaced once every two days, and the nanohydrogels weight was measured on day 1, 3, 5, 7, 14, 21, 28, 35 and 42 after the surface moisture was dried with absorbent paper. The degradation (%) was determined by using the following equation:

$$\text{Degradation(\%)} = \frac{\text{Final weight}}{\text{Initial weight}} \times 100 \quad (2)$$

#### Cell culture

Mice neural stem cells (NE-4C, ATCC, CRL-2925) and human neuroblastoma cells (SH-SY5Y, ATCC, CRL-2266) were cultured in low glucose DMEM (Gibco; Thermo Scientific, USA) medium containing 10% FBS (VivaCell, Shanghai, China) and penicillin (100 U/mL) and streptomycin (100 μg/mL) (Invitrogen). Cells were incubated in an incubator at 37 °C and 5% CO<sub>2</sub>. The medium was replaced every other day.

#### Cytotoxicity of nanocomposite hydrogels

The cytotoxicity of nanocomposite hydrogels against NE-4C was assessed using Cell Counting Kit 8 (CCK-8) (Dojindo Laboratories, Kumamoto, Japan). NE-4C cells were seeded in 96-well plates with a density of 4 × 10<sup>4</sup> cells per well. Different concentrations of MoS<sub>2</sub>, GO, and MoS<sub>2</sub>/GO NSs (500, 250, 125, 62.5, 31.25, 15.6, 7.8, 0 μg/mL) were added to cells after 24 h. After cocultured for another 24 h, the CCK-8 assay was taken to evaluate their toxicity. Additionally, the proliferation rate of PVA, MoS<sub>2</sub>/PVA, GO/PVA, and MoS<sub>2</sub>/GO/PVA hydrogels was measured using CCK-8 assay after cocultured with NE-4C cells for 24 h.

#### Live/dead staining

0.1 g PVA, MoS<sub>2</sub>/PVA, GO/PVA, and MoS<sub>2</sub>/GO/PVA hydrogels were firstly added to the 24-well plate, then NE-4C cells were seeded in the wells with a density of 1 × 10<sup>5</sup> cells. After 24 h culture, a live/dead staining kit (BestBio, Shanghai, China) was applied to different treatment groups, and the images were obtained

using a Leica DMI3000B inverted microscope (Leica, Germany). The quantitative analysis of living and dead NE-4C cells was conducted by ImageJ2x (Rawak Software, Germany).

### Hemolysis tests

5 mL Blood was obtained from the mice. Blood was placed in a triangular bottle with glass beads and slightly stirred to remove fibrin. Then the blood was centrifuged with normal saline till the supernatant was colorless and transparent, and then the washed red blood cells were mixed with normal saline into 2% of cell suspension for later use. GO/PVA, MoS<sub>2</sub>/PVA, and MoS<sub>2</sub>/GO/PVA were prepared with normal saline at concentrations of 500, 250, 125, and 62.5 µg/mL, and 10 mg of composite hydrogels were immersed in 0.8 mL normal saline for incubation at 37 °C for 1 h. 0.8 mL ddH<sub>2</sub>O and PBS were set as positive control and negative control, respectively. Afterwards, 0.2 mL of diluted erythrocyte suspension was added to each sample and incubated at 37 °C for 1 h. After that, all samples were centrifuged at 3000 rpm for 5 min and the supernatant was collected. The O.D. of the supernatant was measured at 545 nm using a microplate analyzer. The hemolytic percentage was calculated using the following formula:

$$\text{Hemolysis rate (\%)} = \frac{\text{O.D. Sample} - \text{O.D. Negative control}}{\text{O.D. Positive control} - \text{O.D. Negative control}} \times 100 \quad (3)$$

### Neural cell differentiation

In order to make the cells better enter the state of preparation for the following induction of differentiation, we changed the medium of NE-4C and SH-SY5Y cells into serum-free DMEM/F12 (Gibco, Thermo Scientific, USA) containing 1% penicillin–streptomycin, 1% B-27 supplement, and 5 µM retinoic acid (RA). The NE-4C and SH-SY5Y cells were respectively cocultured with different hydrogels for 3 and 7 days, and then the phenotype of neural cell differentiation was detected by immunofluorescence and PCR.

### Immunostaining fluorescence

0.1 g PVA, MoS<sub>2</sub>/PVA, GO/PVA, and MoS<sub>2</sub>/GO/PVA hydrogels were firstly added to the 24-well plate, then NE-4C cells were seeded in the wells with a density of 1 × 10<sup>5</sup> cells. After being cocultured with different hydrogels for 3 and 7 days, the cells were fixed with 4% formaldehyde on ice for 15 min. After being washed with PBS, the cells were incubated in 0.5% TritonX-100 and diluted by PBS at room temperature for 20 min. After being washed with PBS, the cells were sealed at room temperature in 5% of BSA for 1 h. Then, primary antibodies

anti-Tuj1 (GTX108731, 1:500; Genetex) and GFAP (GTX108711, 1:500; Genetex) diluted in 1% of BSA solution was added to the cells and incubated overnight at 4 °C. The cells were rewashed with PBS and incubated with DyLight 488 goat anti-mouse IgG (diluted 1000 times in 5% BSA, Biodragon) and Alexa Fluor 633 binding goat anti-rabbit IgG (diluted 1000 times in 5% BSA, Biodragon). After being incubated for 30 min at 37 °C in a dark environment, the secondary antibodies were washed. The nuclei were stained with DAPI dye, and the images were captured using a ZEISS LSM 900 confocal microscope (ZEISS, Germany).

### Gene expression analysis

The RNA in PVA, MoS<sub>2</sub>/PVA, GO/PVA, and MoS<sub>2</sub>/GO/PVA hydrogels treated groups was extracted by RNA extraction kit (R4114-02, Magen, China), and RNA was reversely transcribed into cDNA by reverse transcription kit (11939823001, Roche, Switzerland). RT-PCR was performed using Maxima TM SYBR Green/Rox qPCR Master Mix (4710436001, Roche, Switzerland). Each individual PCR assay was repeated at least three times, and the expression of GAPDH was used to calculate the expression level of each detected gene. 2<sup>-ΔΔ</sup> quantitative Ct method was used to calculate relative gene expression.

The primers used in this study are listed in Table 1.

### ROS detection in NE-4C cells

ROS in NE-4Cs after 24 h seeded on GO/PVA, MoS<sub>2</sub>/PVA and MoS<sub>2</sub>/GO/PVA hydrogels was detected by reactive oxygen species detection kit (ab113851, Abcam, China), in which DCFH-DA was diluted to the final

**Table 1** Primers sequence used for real-time PCR

Target	Forward	Reverse
GAPDH	AGGTCGGTGTGAACGGATTTG	GGGGTCGTTGATGGCAACA
GFAP	CGGAGACGCATCACCTCTG	TGGAGGAGTCATTGAGACAA
HB9	GAACACCAGTTCAAGCTC	GCTGCGTTTCCATTTTCATTG
Isl-1	TTTCCCTGTGTGTTGTTGC	TGATTACACTCCGCACATTTC
ChAT	GGCCATTGTGAAGCGGTTTG	GCCAGGCGGTTGTTTAGATACA
Tuj1	TAGACCCAGCGGCAACTAT	GTTCCAGGTTCCAAGTCCACC
IL-10	TTGTCCGTTTGTCTCCATT	GAAGGGCTTGGCAGTTCTG
IL-6	TGGGGCTCTTCAAAGCTCC	AGGAACATACCCGGATC TTCAA
TNF-α	CAGGCGGTGCCTATGCTC	CGATCACCCCGAAGTTCAGTAG

concentration of 10  $\mu\text{mol/L}$  in serum-free medium at 1:1000. The cell culture medium was removed, and 200  $\mu\text{L}$  DCFH-DA (1:1000) was added. The fluorescence images were captured using a fluorescence microscope (DMI3000B, Leica, Germany).

#### Flow cytometry

0.1 g PVA,  $\text{MoS}_2/\text{PVA}$ ,  $\text{GO}/\text{PVA}$ , and  $\text{MoS}_2/\text{GO}/\text{PVA}$  hydrogels were firstly added to the 24-well plate, then NE-4C cells were seeded in the wells with a density of  $1 \times 10^5$  cells. Then 100 ng/mL lipopolysaccharide (LPS) (L4391-1 mg, Sigma-Aldridge) were added to the culture for 24 h, and cells were then collected, washed twice with cold PBS, stained with FITC anti-mouse CD206 (141703 Biologend, USA) and PE anti-mouse CD11c (101307, Biologend, USA) in the binding buffer for 30 min, and then detected by flow cytometry (FACS Calibur flow cytometry; BD Biosciences). FlowJo-V10 software was used to analyze the proportion of M1 and M2 macrophages in each group.

#### SCI model in mice

All aspects of animal experiments were approved by the Ethical Committee of Laboratory Animals of General Hospital of Southern Theater Command of PLA. Male C57BL/6 N mice were aged 6–8 weeks old and purchased from Guangdong Medical Laboratory Animal Center. The animals were randomly divided into five groups: Sham, SCI,  $\text{GO}/\text{PVA}$ ,  $\text{MoS}_2/\text{PVA}$ , and  $\text{MoS}_2/\text{GO}/\text{PVA}$  ( $n=15$ ). C57 mice were anesthetized by intraperitoneal injection with 4 mL/kg 10% chloral hydrate. After skin preparation, iodophor was used to disinfect the skin of the operation area. Skin soft tissues were cut at the T9-10 level to expose the spine, and the lamina was cut to expose the spinal cord. 2 mm of the spinal cord was removed on the right side. The hydrogels of the same size were implanted. The surgical incision was sutured layer by layer, only the spinal cord was exposed in the Sham operation group, and no hydrogel was implanted after spinal cord resection in the SCI group.

#### Histological staining

Six weeks after the operation, the C57 mice were sacrificed by neck-breaking, the surgical area and the surrounding spinal cord were removed, the tissue samples were quickly fixed with 4% paraformaldehyde for 24 h, and then washed with PBS for three times and 50% alcohol for twice, followed by ethanol gradient dehydration and paraffin-embedded tissues. The xylene transparent tissues were repaired, and the embedded tissue block was cut into paraffin tape of 4  $\mu\text{m}$  with a slicer. After being

stained with hematoxylin and eosin (H&E), the images were observed under Olympus BX51 light microscope.

#### Immunohistochemistry staining

Immunohistochemistry was used to evaluate the effects of nanocomposite hydrogels on the differentiation of neonatal spinal cord tissue in vivo. Tissue sections from the same wax block used for H&E staining were taken for immunohistochemistry staining. After routine dewaxing and rehydration, the antigen was repaired with 3%  $\text{H}_2\text{O}_2$ . They were sealed with goat serum at 37 °C for 30 min. The samples were then incubated overnight with primary antibodies: rabbit anti-HB9 antibody (ORB157435, 1:1000, Biorbyt), rabbit anti-Islet-1 antibody (GTX 102807, 1:1000, Genetex), rabbit anti-ChAT antibody (PA5, 1:10000, Thermo Fisher), rabbit anti-GFAP antibody (GTX108711, 1:1000, Genetex), and rabbit anti-Tuj1 (GTX130245, 1:1000, Genetex) at 4 °C. After being washed with PBS, the samples were incubated with goat anti-rabbit IgG secondary antibody (ab6747, Abcam, China) at 37 °C for 10 min. The being colorized by the chromogenic agent, the sections were re-dyed with hematoxylin and eosin. They were dehydrated, sealed, observed, and photographed under a light microscope (Olympus BX51, Japan).

#### Functional assessment

Basso, Beattie and Bresnahan (BBB) score was applied to evaluate the recovery of hind limb motor function in mice. Firstly, mice were placed in an open and flat place, and their movements were observed and recorded. The full score of the three items was 21 points, which were evaluated by the movements of the hind limbs, the gait and coordination function of the hind limbs, and the fine movements of the claws in the movement. The animals were evaluated weekly. The graders were conducted by three people blindly. Secondly, after the front and rear feet of mice were marked with black and red dyes, they were placed in a track covered with white paper in advance to make the animals run from one end to another. The inter limb coordination of the center of the front and rear feet of mice on the same side and the angle of rotation of the third foot of the hind limb were observed for analysis.

#### Western blot

The collected spinal cord tissue samples were quickly frozen in liquid nitrogen, where the tissue was ground until there were no obvious tissue particles. Electrophoresis gel was prepared using a gel preparation kit (Beyotime, Shanghai, China) to isolate total protein of spinal cord tissue. Rapid membrane transfer apparatus

(Bio-Rad, USA) was used to transfer the isolated protein onto a polyvinylidene fluoride (PVDF) membrane. The PVDF membrane was sealed with 5% skim milk powder and prepared by PBS for 1 h. Then, the membrane was incubated with primary antibodies: rabbit anti-HB9 antibody (ORB157435, 1:1000, Biorbyt), rabbit anti-Islet-1 antibody (GTX 102807, 1:1000, Genetex), rabbit anti-ChAT antibody (PA5, 1:10000, Thermo Fisher), rabbit anti-GFAP antibody (GTX108711, 1:1000, Genetex), and rabbit anti-Tuj1 (GTX130245, 1:1000, Genetex) at 4 °C overnight. The horseradish peroxidase labeled sheep anti-rabbit secondary antibody (ab205718, Abcam, China) was incubated at room temperature for 1 h, and the ECL luminescence kit (WBKLS0100, Millipore, USA) was used for luminescence determination. The gray value of each strip was calculated and analyzed by using Image J software.

### Statistical analysis

All statistical analyses in this study were performed using IBM SPSS (version 23.0). All data are represented as mean  $\pm$  SD, and the number of duplicate legends is represented as “n” in the legend. One-way analysis of variance (ANOVA) was used for comparison between the groups at a single time point. Comparison between the two groups at multiple time points was performed using two-way ANOVA, followed by multiple post-hoc comparisons (Dunnett-t test). \*  $p < 0.05$ , \*\*  $p < 0.01$ .

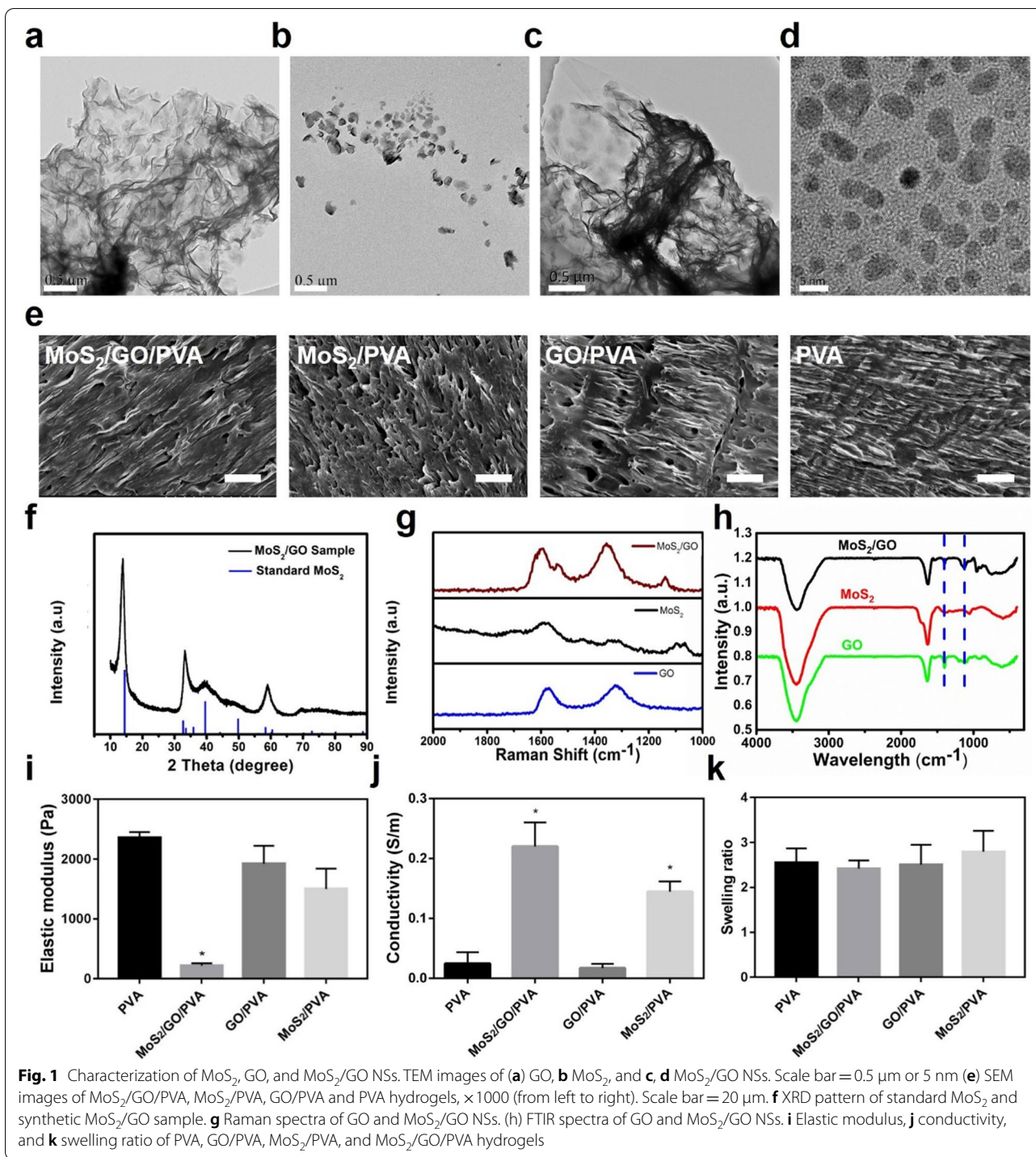
## Results and discussion

### The synthesis and characterization of MoS<sub>2</sub>/GO/PVA

Briefly, MoS<sub>2</sub>/GO NSs was synthesized by a hydrothermal method, and the MoS<sub>2</sub>/GO PVA composite hydrogel was obtained from repeated freezing and thawing. HRTEM image showed that the translucent GO (Fig. 1a), MoS<sub>2</sub> (Fig. 1b), and MoS<sub>2</sub>/GO NSs (Fig. 1c, d). The image of MoS<sub>2</sub>/GO NSs at high magnification displayed that MoS<sub>2</sub> NSs were scattered to GO NSs. The surface morphology and microstructure of the prepared hydrogels were analyzed by SEM (Fig. 1e). MoS<sub>2</sub>/GO/PVA, MoS<sub>2</sub>/PVA, GO/PVA, and PVA hydrogels were well arranged with gap structure. The SEM results showed that the surface of hydrogels in each group was evenly and neatly spaced, and no obvious granular substance was found, indicating that nanoparticles were well dispersed in PVA hydrogels. GO NSs, here, have good dispersibility in PVA hydrogel [15, 16] and will further better optimize various properties of hydrogels [17]. The XRD pattern (Fig. 1f) indicated that the peaks of MoS<sub>2</sub>/GO were well indexed to the standard MoS<sub>2</sub> crystal phases (JCPDS 74-0932), suggesting that MoS<sub>2</sub> NSs successfully synthesized on GO NSs. Raman spectra (Fig. 1g) of GO showed the characteristic G band at 1580 cm<sup>-1</sup> and D band at

1320 cm<sup>-1</sup>. Correspondingly, the G band of MoS<sub>2</sub>/GO NSs was peaked at 1600 cm<sup>-1</sup>, and the D band shifted slightly to 1360 cm<sup>-1</sup>, which illustrated the existence of GO in MoS<sub>2</sub>/GO NSs. The FTIR spectra of the MoS<sub>2</sub>/GO, MoS<sub>2</sub>, and GO NSs were shown in Fig. 1h. It can be seen that the FTIR spectra of MoS<sub>2</sub> are very similar to MoS<sub>2</sub>/GO because of their similar organic compositions (C, H, O in all samples). Briefly, the broad vibration peak at 3200–3600 cm<sup>-1</sup> is attributed to the hydroxyl/H<sub>2</sub>O in the NSs. Furthermore, the –OH bonding could be found at 1600–1700 cm<sup>-1</sup> for all samples. The stretching vibration of CH<sub>2</sub> and C–O bonds could also be found in 1000–1200 cm<sup>-1</sup> and 1400 cm<sup>-1</sup>. HAADF-STEM was employed to conduct the elemental distribution of Mo, S, C, and O elements in the nanocomposite (Additional file 1: Fig. S1) and thus proven the abovementioned chemical elements in the MoS<sub>2</sub>/GO NSs. In addition, X-ray photoelectron spectroscopy (XPS) was conducted to study the elemental compositions, properties, and valence states of the MoS<sub>2</sub>/GO. As could be seen from Additional file 1: Fig. S2, the characteristic peaks at 231.62 eV, 161.87 eV, 285.03 eV, 531.22 eV in XPS spectra were well matching to Mo 3d, S 2p, C 1 s, and O 1 s, respectively, which further confirmed that MoS<sub>2</sub> NSs was anchored on GO NSs in MoS<sub>2</sub>/GO NSs. After a series of characterization analysis and optimization, MoS<sub>2</sub> and GO with the molar ratio of 1:2.28 were finally selected to synthesize MoS<sub>2</sub>/GO NSs. Moreover, since TMB can be oxidized to a blue product in the exist of catalyst, POD-like activities of GO, MoS<sub>2</sub>, and MoS<sub>2</sub>/GO NSs were detected by TMB-H<sub>2</sub>O<sub>2</sub> reaction (Additional file 1: Fig. S3) [18–20]. The results manifested that MoS<sub>2</sub>/GO NSs possessed higher POD-like activities than GO and MoS<sub>2</sub> NSs, which were consistent with previous evidence about MoS<sub>2</sub>/GO [21]. Reportedly, MoS<sub>2</sub> NSs-based system exhibited intrinsic antioxidant properties including POD-, superoxide dismutase (SOD)-, and catalase (CAT)-like activities, which could efficiently scavenge ROS including superoxide anion (O<sub>2</sub><sup>-</sup>), hydroxyl radicals ( $\cdot$ OH), and H<sub>2</sub>O<sub>2</sub> [18, 22]. Here, we proved that MoS<sub>2</sub>/GO NSs exhibited the highest catalytic efficiency. The detailed mechanism should be that, GO NSs have high vacancy defects and hole defects because of their over oxidation [23], the defects enhance the rapid electron transfer as well as high conductivity after reacting with MoS<sub>2</sub>, resulting in the high catalytic ability of MoS<sub>2</sub>/GO NSs [21, 22].

Furthermore, compared with PVA hydrogels at different weights in volume from 2.5% to 15% (w/v), compound hydrogels containing 10% (w/v) PVA exhibited the closest strength to the spinal cord and good adhesion (Additional file 1: Fig. S4). Therefore, 10% PVA was selected as the host hydrogels in the subsequent experiments. After being combined with GO, the zeta potential of MoS<sub>2</sub>/



PVA changed from -10.5 mV to -33 mV (Additional file 1: Fig. S5), suggesting the enhancement of MoS<sub>2</sub>/GO/PVA stability.

Hydrogels could promote the proliferation of neural stem cells at the elastic modulus of 183-19700 Pa, and the lower the elastic modulus, the higher the

proliferation rate [24]. As shown in Fig. 1i, the elastic modulus of experimental groups were 2361.99 Pa for PVA, 1500.24 Pa for GO/PVA, 1923.69 Pa for MoS<sub>2</sub>/PVA, and 220.07 Pa for MoS<sub>2</sub>/GO/PVA, which were all in the range of 183-19700 Pa. Notably, the elastic modulus of MoS<sub>2</sub>/GO/PVA is significantly lower (p < 0.05) than



that of PVA, GO/PVA and MoS<sub>2</sub>/PVA. Previous studies showed that the mechanical properties of PVA could be enhanced by adding conductive nanoparticles [25], the lower elastic modulus may reduce the growth resistance of the spinal cord after SCI [24].

Electrical signaling among nerve cells is important for the maintenance of the nervous system and the recovery of the musculoskeletal motor system [26]. As shown in Fig. 1j, the average electrical conductivity of PVA, GO/PVA, MoS<sub>2</sub>/PVA, and MoS<sub>2</sub>/GO/PVA were 0.025, 0.028, 0.131, and 0.220 S/m, the average electrical conductivity of MoS<sub>2</sub>/PVA and MoS<sub>2</sub>/GO/PVA were significantly higher than that of GO/PVA and PVA ( $p < 0.05$ ). Previous literature reported that the electrical conductivity of spinal cord tissue is between 0.08 and 0.23 S/m [27], the synthesized MoS<sub>2</sub>/GO/PVA with good conductivity is favorable for the connection of neurons, which is beneficial for the further repair of SCI. Moreover, we have detected the photoelectric effect of MoS<sub>2</sub>/GO and GO (Additional file 1: Fig. S7). In the cycle of 40 s light stimulation, the instantaneous current of MoS<sub>2</sub>/GO NSs could reach  $5.2 \times 10^{-5}$  A, while GO NSs were not detected significant current. The result indicated that MoS<sub>2</sub>/GO NSs play a key role in the electrical conductivity of the MoS<sub>2</sub>/GO/PVA, this could be related to the well semiconductor properties of MoS<sub>2</sub> [28]. Additionally, improved conductivity of MoS<sub>2</sub>/GO/PVA might be attributed to increased two-dimensional order of MoS<sub>2</sub>/GO NSs caused by the combination of MoS<sub>2</sub> and GO NSs [29].

The swelling rates of GO/PVA, MoS<sub>2</sub>/PVA, MoS<sub>2</sub>/GO/PVA, and PVA nanocomposite hydrogels were 2.55 for PVA, 2.51 for GO/PVA, 2.80 for MoS<sub>2</sub>/PVA, and 2.42 for MoS<sub>2</sub>/GO/PVA after 24 h, respectively (Fig. 1k). There was no significant difference in swelling rate among the four hydrogels, which indicated that their capacities of transporting small molecules were similar [30].

The degradation of the nanohydrogels was studied in the SBF for about six weeks. The PVA, MoS<sub>2</sub>/PVA, GO/PVA, and MoS<sub>2</sub>/GO/PVA hydrogels exhibited a similar trend in SBF solutions. As shown in Additional file 1: Fig. S8, they degraded rapidly in the first week (up to 40%), then the degradation trend to slow and all the hydrogels tended to degrade about 70% in the 42 days.

#### Biosafety of nanocomposite hydrogels in vitro

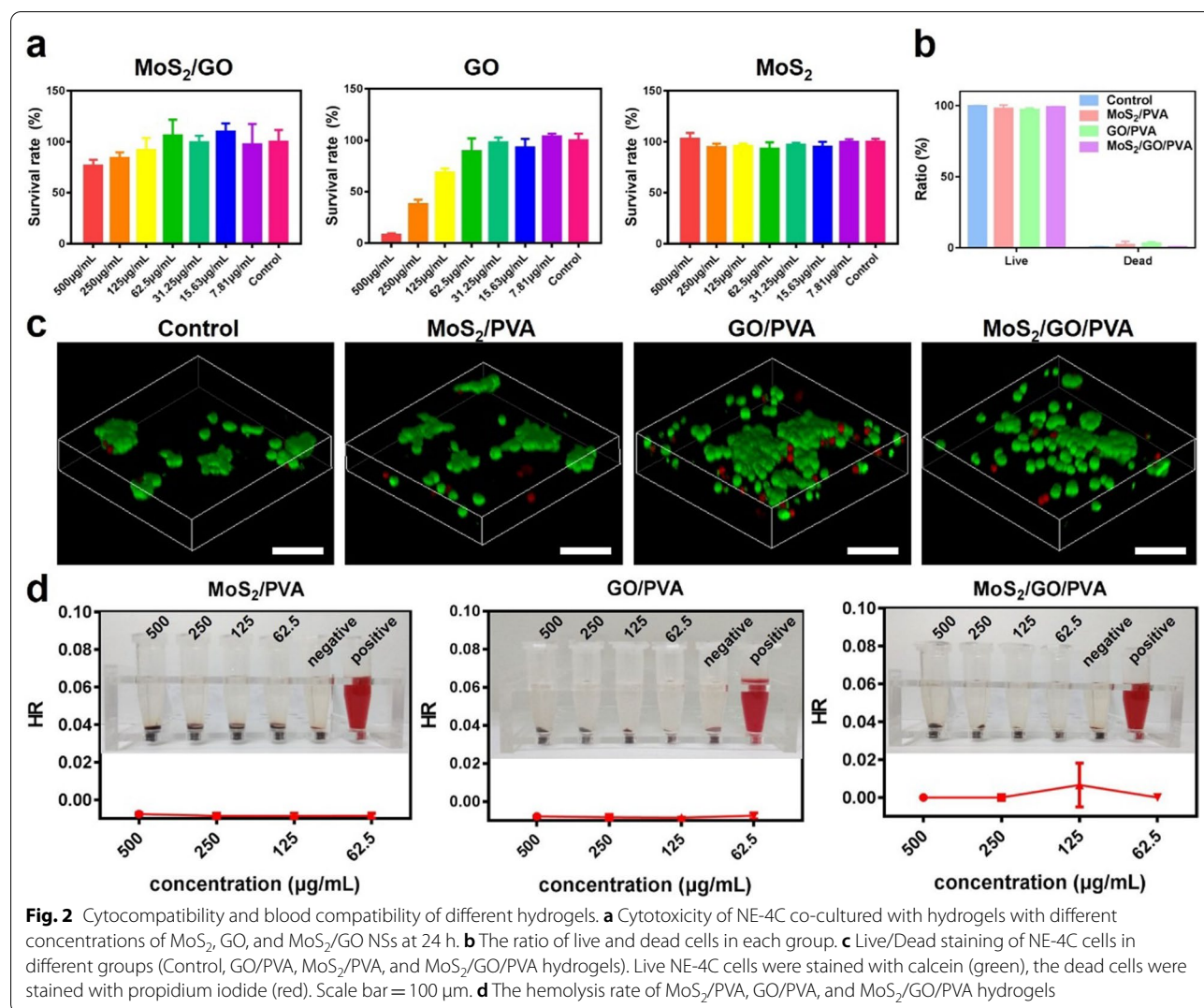
Good biocompatibility is the most basic condition for the application of biomaterials [31]. We assessed the cytotoxicity of GO/PVA, MoS<sub>2</sub>/PVA, and MoS<sub>2</sub>/GO/PVA toward NE-4C by using CCK-8 (Fig. 2a). When their concentrations were below 62.5 µg/mL, the survival rates of GO/PVA, MoS<sub>2</sub>/PVA, and MoS<sub>2</sub>/GO/PVA groups were all above 85%, exhibiting low cytotoxicity. Thus, MoS<sub>2</sub>/GO, GO, and MoS<sub>2</sub> at concentrations of 62.5 µg/mL were

selected for the subsequent experiments. The NE-4C cell proliferation was further detected using CCK-8 assay in hydrogels of different components, and there was no significant difference in the proliferation rate of different hydrogels after 24 h of coculture (Additional file 1: Fig. S9). Live/dead staining was further applied in NE-4C to verify the cytotoxicity of GO/PVA, MoS<sub>2</sub>/PVA, and MoS<sub>2</sub>/GO/PVA (Fig. 2b, c). After cocultured with the above materials for 24 h, almost all the NE-4C cells were alive (green fluorescence) on the hydrogels, and the quantitative analysis of living and dead cells further indicated their good biocompatibility.

Blood compatibility is important to evaluate the biocompatibility of biomaterials [32]. As shown in Fig. 2d, the supernatant of all material groups and negative control (phosphate buffer saline, PBS) groups were clear, and they did not show obvious red color. In contrast, the supernatant of the positive control (double distilled water, dd H<sub>2</sub>O) turned distinct red color due to the release of hemoglobin from the broken red blood cells. The hemolysis rates of each material group were all significantly lower than 5%.

#### Effects of nanocomposite hydrogels on neural cells differentiation

Encouraged by the excellent biosafety of the composite hydrogels, we further studied their effects on neural cells growth and differentiation, which is highly related to the process of spinal cord repair [33]. Neural stem cells [34] and neuroblastoma cells [35] both have the potential to differentiate into both nerve cells and glial cells. In order to verify the differentiation effect of nanohydrogels on neural cells of different species. NE-4C and SH-SY5Y cells were cocultured with nanohydrogels to detect their direction of differentiation. Here, neuronal-specific marker protein class III beta tubulin (Tuj1) and astrocytes specificity of collagen fiber acidic protein (GFAP) were applied to detect the fate of neural cells differentiation after cocultured with different hydrogels. By confocal microscope (Fig. 3a–c), we found that the expression of neuron-specific Tuj1 in control, GO/PVA, and MoS<sub>2</sub>/PVA groups were significantly lower than MoS<sub>2</sub>/GO/PVA group. In addition, we also found that Tuj-1 positive SH-SY5Y cells in the MoS<sub>2</sub>/GO/PVA group grew a large number of tentacles in all directions, while this phenomenon was not found in other groups. Glial cells are the main components of nerve scars and important factors that hinder the repair of nerve tissue [36]. GFAP is the main marker of glial cells, and we next investigated the expression of GFAP among all groups. As expected, MoS<sub>2</sub>/GO/PVA inhibited the expression of GFAP, and the red fluorescence in the MoS<sub>2</sub>/GO/PVA group was weaker than other groups after 3 days and 7 days. It was found that MoS<sub>2</sub>/GO/PVA could



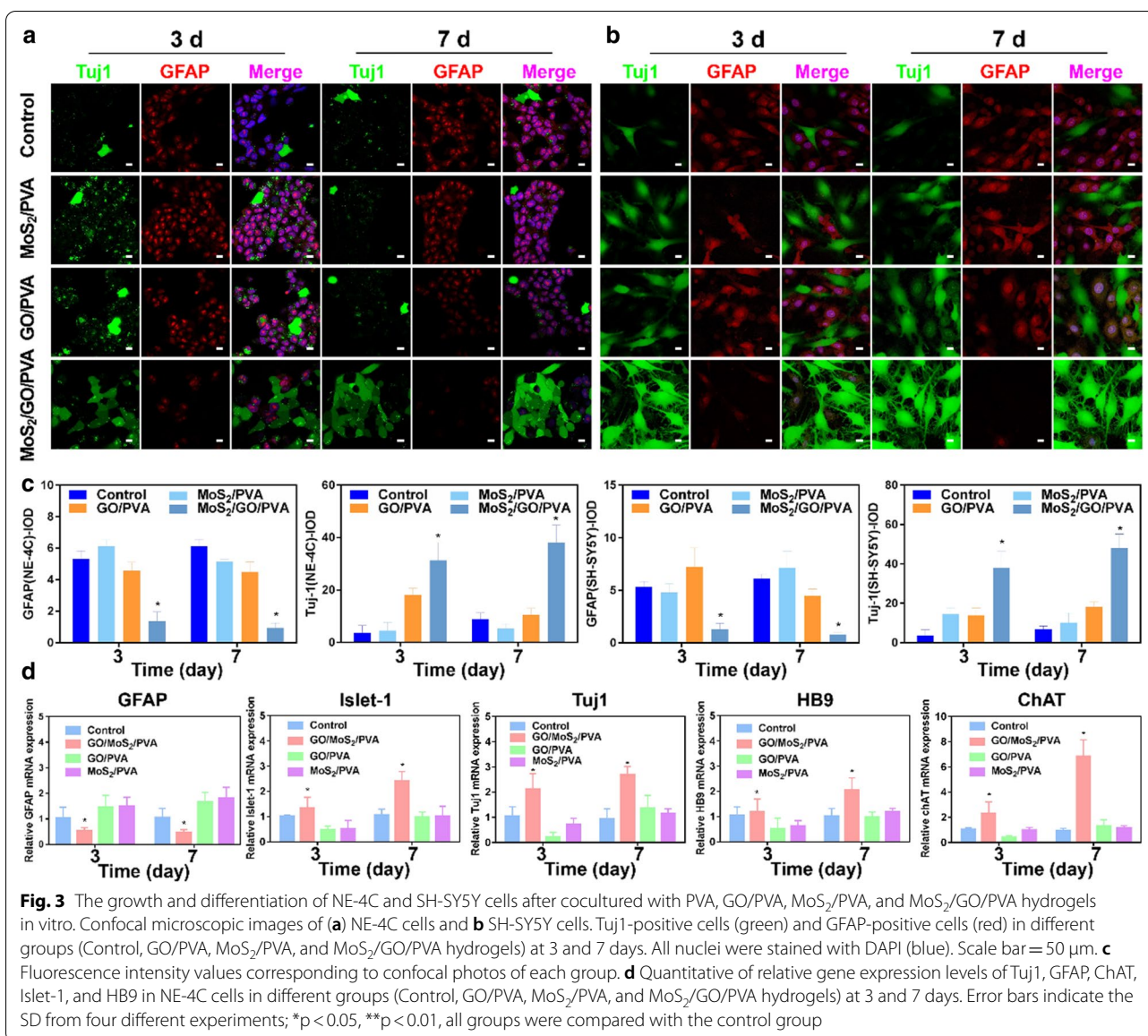
promote the differentiation of neural stem cells into neural cells more effectively than other hydrogels. Interestingly, the conductivity of MoS<sub>2</sub>/GO/PVA was also the highest among all groups. Previous studies have also shown the close relationship between neural differentiation and electrical conductivity of the cells [37, 38]. Moreover, their excellent biocompatibility matched Young's modulus, and ROS quenching ability may also benefit neural differentiation. Therefore, this test indicated that MoS<sub>2</sub>/GO/PVA composite hydrogels have great advantages in promoting nerve cells growth and differentiation.

We further examined the represent genes changes of NE-4C cells in different treatment groups. As shown in Fig. 3d, Tuj1, Choline acetyltransferase (ChAT), motor neuron markers Islet-1, and the HB9 expression in MoS<sub>2</sub>/GO/PVA hydrogel group were significantly higher ( $p < 0.05$ ) than that on other groups. In contrast, the

expression of GFAP in the MoS<sub>2</sub>/GO/PVA hydrogel group was significantly decreased ( $p < 0.05$ ) than in other groups. Overall, the quantitative reverse transcription polymerase chain reaction (RTqPCR) test on Tuj1, ChAT, Islet-1, and the HB9 expression further confirmed the promotion of nerve growth factor and inhibition of the glia growth factor, which was in accord with the fluorescence images. The above results indicated that MoS<sub>2</sub>/GO/PVA hydrogel promoted the NE-4C cells to differentiate into nerve cells and inhibited glial cell differentiation, which may attribute to MoS<sub>2</sub>/GO/PVA hydrogel's characteristics of high conductivity [39] and low elastic modulus [24].

#### Inhibitory effects of nanocomposite hydrogels on the secondary injury of SCI

ROS is one of the major factors produced in the secondary injury after SCI. In order to test the effects of



composite hydrogel on the secondary injury after SCI, we tested the ROS level using dichloro-dihydro-fluorescein diacetate (DCFH-DA) in NE-4C cells. In Fig. 4a and b, the NE-4C cells in the MoS<sub>2</sub>/GO/PVA group showed the weakest fluorescent intensity and lowest ROS level compared with other groups, we used the same method to detect the effect of hydrogels on ROS levels in RAW264.7 cells, and the results were consistent with those in NE-4C cells (Additional file 1: Fig. S10), indicating that the MoS<sub>2</sub>/GO/PVA hydrogel could effectively inhibit the production of ROS.

Macrophages begin to increase rapidly in the SCI part after 1–2 days due to the serious inflammatory [40]. Their polarization ratio is highly related to SCI recovery. Here, we employed flow cytometry to detect

the proportion of macrophages with different polarization directions after cocultured with different hydrogel groups (Fig. 4c and d). Macrophages were in a state of inflammation after being stimulated by LPS, then after cocultured with nanohydrogel for 24 h, MoS<sub>2</sub>/GO/PVA group showed the highest M2 ratio in Fig. 4c, indicating that MoS<sub>2</sub>/GO/PVA nanohydrogel can effectively reverse the transformation of M1 into M2, thus inhibiting the secondary injury caused by the excessive concentration of M1 in SCI.

We next detected the inflammatory cytokines, including IL-6, IL-10, and TNF- $\alpha$ , in different groups (Fig. 4e). The expression of protective cytokine IL-10 was relatively higher in the MoS<sub>2</sub>/GO/PVA group than the other three groups. In contrast, the pro-inflammatory mediators IL-6

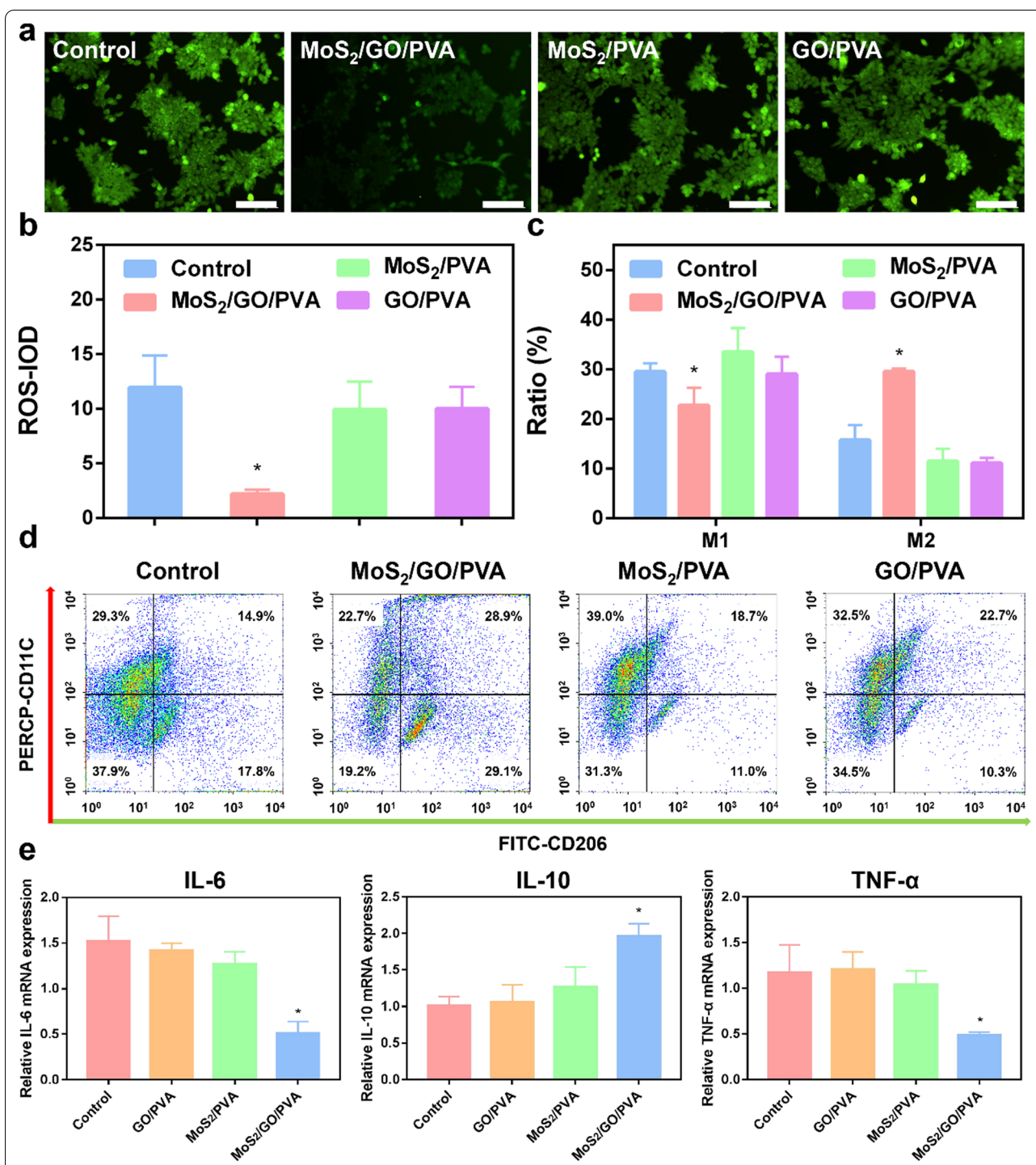


**Fig. 4** ROS scavenging and anti-inflammatory properties of MoS<sub>2</sub>/GO/PVA hydrogel. **a** The effect of PVA (set as control), GO/PVA, MoS<sub>2</sub>/PVA, and MoS<sub>2</sub>/GO/PVA hydrogels on ROS production in H<sub>2</sub>O<sub>2</sub>-induced NE-4C cells. Scale bar = 50 μm. **b** DCF fluorescence intensity of PVA (set as control), GO/PVA, MoS<sub>2</sub>/PVA, and MoS<sub>2</sub>/GO/PVA hydrogels. **c** The M1, M2 macrophage ratio in each group. **d** The flow cytometry images of RAW264.7 cells after cultured with PVA (set as control), GO/PVA, MoS<sub>2</sub>/PVA, and MoS<sub>2</sub>/GO/PVA hydrogels for 24 h. **e** RT-PCR results of IL-6, IL-10, and TNF-α in different treatment groups; \*p < 0.05. \*\*p < 0.01. All groups were compared with the control group

and TNF- $\alpha$  decreased in the MoS<sub>2</sub>/GO/PVA group, indicating that the MoS<sub>2</sub>/GO/PVA hydrogel could inhibit the destructive inflammatory response.

#### Effects of nanocomposite hydrogels on spinal cord repair in vivo

Restoring the electrical conductivity of the spinal cord quickly after SCI will benefit the functional recovery of the spinal cord innervated area [41]. Therefore, we filled the hemisection of the spinal cord in mice with composite hydrogels to study their prothetic effects on the SCI and the subsequent influence on the motor function dominated by the injured area of the spinal cord (Fig. 5a, b). Six weeks after the SCI and transplantation, inflammatory or toxic reactions were not observed in the major visceral organs in all groups. The H&E results indicated that hydrogels transplantation did not cause harm to the main organs of all groups (Additional file 1: Fig. S11), which was also consistent with the results of the in vitro safety studies.

The anterior cord of the spinothalamic descends ipsilaterally and innervates the motor function of the ipsilateral soma [42]. Therefore, ipsilateral motor dysfunction presented in spinal cord hemisection injury. The BBB scale is a classical scale to evaluate the recovery of motor function in laboratory mice [43]. Therefore, we monitored the recovery of motor function of mice after SCI by evaluating BBB scores once a week for 6 weeks after surgery (Fig. 5c). We observed that in the Sham group, motor function remained normal, with a score of 21 through 6 weeks. The SCI, GO/PVA, and MoS<sub>2</sub>/PVA groups had a slight increase after 6 weeks in postoperative BBB scores, but the scores were still below 10 points, and there was no statistical difference among the three groups (Additional file 2: Video S1). But, the scores in the MoS<sub>2</sub>/GO/PVA group at week 4 and week 5 were significantly higher than those of SCI, GO/PVA, and MoS<sub>2</sub>/PVA groups. The results illustrated that the MoS<sub>2</sub>/GO/PVA hydrogel could accelerate the recovery of hind limb motor function of mice after SCI. In addition to scores, footprints can also be observed to promote the motor function of mice after SCI (Fig. 5d). At the 6th week after surgery, drag traces and directional instability traces were found in SCI, GO/PVA, and MoS<sub>2</sub>/PVA groups. In contrast, the mice in the MoS<sub>2</sub>/GO/PVA group showed clear footprints, which further demonstrated

the promoting effects of MoS<sub>2</sub>/GO/PVA hydrogel on the recovery of hind limb motor function in mice. As shown in Fig. 5e 6 weeks after the transplantation, GO/PVA, MoS<sub>2</sub>/PVA, and MoS<sub>2</sub>/GO/PVA groups showed partial spinal cord repair compared to the SCI group. It is noteworthy that in the MoS<sub>2</sub>/GO/PVA group, the nanocomposite hydrogel adhered well to the spinal cord during specimen collection without apparent inflammatory reaction around the material.

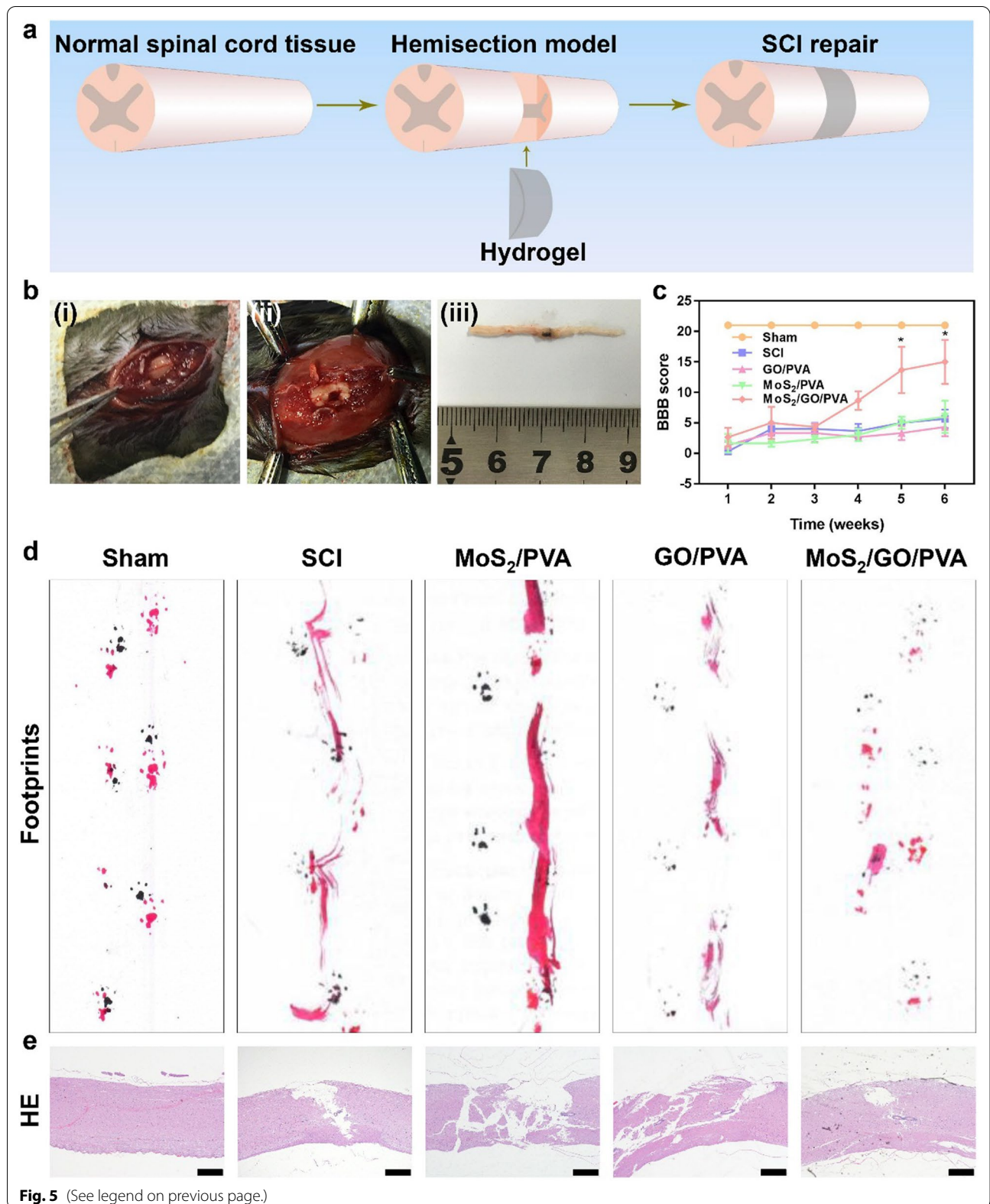
In order to further verify the differentiation direction of spinal cord tissue repair, we tested the spinal cord tissues using immunohistochemistry (IHC) (Fig. 6a, b) and western blotting (WB) (Fig. 6c, d). The expression of glial-related protein GFAP was relatively lower in the sham and MoS<sub>2</sub>/GO/PVA group, while the expression of neurons-related protein Tuj1, HB9, Islet-1, and ChAT was significantly higher than the other groups. In addition, the glia marker GFAP was mainly expressed in the SCI group, GO/PVA group, and MoS<sub>2</sub>/PVA group. The results were consistent with the experimental results of neural stem cell differentiation in vitro, indicating that MoS<sub>2</sub>/GO/PVA could promote neural tissue differentiation in vivo.

#### Conclusion

In summary, we have successfully developed a sort of highly conductive, soft, excellent biocompatible, and anti-inflammatory nanocomposite hydrogel. SCI could be effectively repaired by the composite hydrogel because of its appropriate mechanical property and excellent electrical conductivity, which could quickly restore the continuity and electrical conductivity after SCI. More importantly, the composite hydrogel could promote NE-4C to neuronal differentiation and inhibit the development of astrocytes. The hydrogel exhibit has an excellent anti-oxidative property, which could effectively attenuate the ROS and reduce the M1/M2 macrophage ratio in vitro. Most importantly, the in vivo study also showed that the implantation of composite hydrogel could promote the repair of spinal cord tissue and improve the locomotor function of SCI mice. Hence, our works are of great importance for future biomaterials design and medicinal applications in SCI restoration.

(See figure on next page.)

**Fig. 5** The treatment effects of different hydrogels on SCI mice. **a** Scheme of the surgical process of hemisectioned spinal cord repair with hydrogel. **b** Images of implanting hydrogels during SCI operation. (i) The spinal cord was exposed intra-operatively. (ii) A nanocomposite hydrogel was implanted in SCI intra-operatively. (iii) The spinal cord specimen was obtained at 6 weeks after surgery. **c** BBB scores of mice at 6 weeks after surgery.  $n = 6$  animals in each group. Error bars represent SD. \* $p < 0.05$ ; \*\* $p < 0.01$ . All groups were compared with the SCI group. **d** Representational footprints of Sham, SCI, GO/PVA, MoS<sub>2</sub>/PVA, and MoS<sub>2</sub>/GO/PVA groups. The mouse front paw footprints were black, and the hind paw footprints were red. **e** Representative H&E images of spinal cords of Sham, SCI, GO/PVA, MoS<sub>2</sub>/PVA, and MoS<sub>2</sub>/GO/PVA groups at 6 weeks postoperation, Scale bar = 50  $\mu$ m



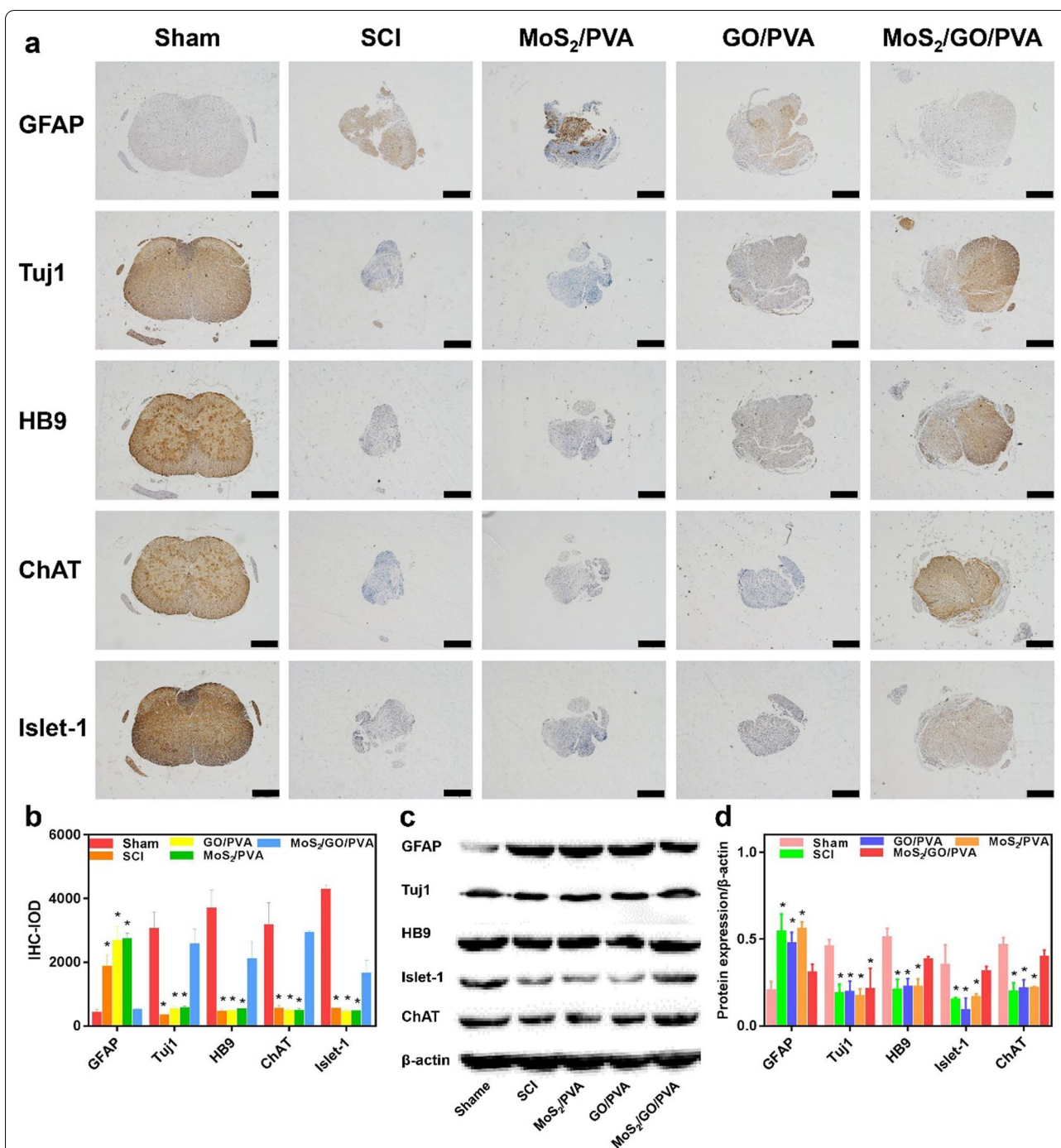


**Fig. 6** Differentiation direction of spinal cord tissue in each group. **a** Representational IHC images of Tuj1, GFAP, ChAT, Islet-1, and HB9 in Sham, SCI, GO/PVA, MoS<sub>2</sub>/PVA, and MoS<sub>2</sub>/GO/PVA groups. The spinal cord tissue of the original defect site was stained with IHC. Due to the difference in the degree of spinal cord repair in each group, there were differences in the area and morphology of immunohistochemistry sections in each group. Scale bars = 50 μm. **b** The IOD value of the IHC images in each group; \*p < 0.05, \*\*p < 0.01. All groups were compared with Sham group. **c** Western blotting bands of Tuj1, GFAP, ChAT, Islet-1, and HB9 of the NE-4C cells in Sham, SCI, GO/PVA, MoS<sub>2</sub>/PVA, and MoS<sub>2</sub>/GO/PVA groups at 6 weeks postoperatively. **d** Gray values of western blotting in each group; \*p < 0.05. All groups were compared with the Sham group

## Supplementary Information

The online version contains supplementary material available at <https://doi.org/10.1186/s12951-022-01396-8>.

**Additional file 1: Fig. S1.** Mapping images of MoS<sub>2</sub>/GO CN. **Fig. S2.** XPS spectra of MoS<sub>2</sub>/GO CN. **Fig. S3.** POD-like properties of GO, MoS<sub>2</sub> and MoS<sub>2</sub>/GO NSs. **Fig. S4.** Adhesion tests of hydrogels to spinal cord tissue in vitro. **Fig. S5.** Zeta potential of nanocomposite hydrogels. **Fig. S6.** Conductivity test of nanocomposite hydrogels in vitro. **Fig. S7.** Photocurrent of PVA, GO/PVA, MoS<sub>2</sub>/PVA and MoS<sub>2</sub>/GO/PVA hydrogels. **Fig. S8.** The degradation of the nanocomposite hydrogels in vitro. **Fig. S9.** The proliferation rate of the nanocomposite hydrogels in vitro. **Fig. S10.** Effects of hydrogels on ROS level in RAW264.7 cells. **Fig. S11.** Safety test of nanocomposite hydrogels in vivo.

**Additional file 2: Video S1.** The motor function of each experimental group 6 weeks after the operation.

### Acknowledgements

This study was supported by the National Natural Science Foundation of China (52002133, 81972080), Guangdong Basic and Applied Basic Research Foundation (2019A1515110328), the Research Program of PLA (20QNPY083), the Science and Technology Planning Project of Guangdong Province (2017B030314139), the Natural Science Foundation of Guangdong Province (2015A030312004), the Science and Technology Planning Project of Guangzhou (202102080527, 202002030304), Medical research foundation of Guangdong province (A2019228), Intramural technology program of Southern Theater Command General Hospital (2021NZC030).

### Author contributions

LL and TZ designed the concept and supervised the project. LC, WW, ZL, YL, HC, BL and ZL performed the experiments and analyzed the data. LC and WW wrote the manuscript. HX, LL and TZ revised the manuscript. All authors read and approved the final manuscript.

### Availability of data and materials

All the original data are available upon reasonable request for correspondence authors.

### Declarations

#### Ethics approval and consent to participate

This work was approved by the ethics committee of the General Hospital of Southern Theater Command of PLA.

#### Competing interests

The authors declare no conflict of interest.

#### Author details

<sup>1</sup>Guangdong Key Lab of Orthopedic Technology and Implant Materials, Key Laboratory of Trauma & Tissue Repair of Tropical Area of PLA, Orthopedic Center, General Hospital of Southern Theater Command of PLA, Guangzhou 510010, Guangdong, China. <sup>2</sup>The Second Clinical Medical College, Guangzhou University of Chinese Medicine, Guangzhou 510405, Guangdong, China. <sup>3</sup>Southern Medical University, 1023 South Shatai Road, Guangzhou 510515, Guangdong, China. <sup>4</sup>Department of Orthopedics, Clinical Research Centre, Zhujiang Hospital, Southern Medical University, 253 Gongye Road, Guangzhou 510282, Guangdong, China. <sup>5</sup>Department of Applied Physics, The Hong Kong Polytechnic University, Kowloon 999077, Hong Kong, China.

Received: 17 September 2021 Accepted: 23 March 2022

Published online: 06 May 2022

## References

- Harkema S, Gerasimenko Y, Hodes J, Burdick J, Angeli C, Chen Y, Ferreira C, Willhite A, Rejc E, Grossman RG. Effect of epidural stimulation of the lumbosacral spinal cord on voluntary movement, standing, and assisted stepping after motor complete paraplegia: a case study. *Lancet*. 2011;377:1938–47.
- Fehlings MG, Tetreault LA, Wilson JR, Kwon BK, Burns AS, Martin AR, Hawrylyuk G, Harrop JS. A clinical practice guideline for the management of acute spinal cord injury: introduction, rationale, and scope. *Glob Spine J*. 2017;7:845–945.
- James SL, Theadom A, Ellenbogen RG, Bannick MS, Montjoy-Venning W, Lucchesi LR, Abbasi N, Abdulkader R, Abraha HN, Adsuar JC. Global, regional, and national burden of traumatic brain injury and spinal cord injury, 1990–2016: a systematic analysis for the global burden of disease study 2016. *Lancet Neurol*. 2019;18:56–87.
- Gazdic M, Volarevic V, Harrell CR, Fellabaum C, Jovicic N, Arsenijevic N, Stojkovic M. Stem cells therapy for spinal cord injury. *Int J Mol Sci*. 2018;19:1039.
- López-Dolado E, González-Mayorga A, Gutiérrez MC, Serrano MC. Immunomodulatory and angiogenic responses induced by graphene oxide scaffolds in chronic spinal hemisection rats. *Biomaterials*. 2016;99:72–81.
- Feng Z, Yan K, Shi C, Xu X, Wang T, Li R, Dong W, Zheng J. Neurogenic differentiation of adipose derived stem cells on graphene-based mat. *Mater Sci Eng, C*. 2018;90:685–92.
- Reddy S, He L, Ramakrishana S, Luo H. Graphene nanomaterials for regulating stem cell fate in neurogenesis and their biocompatibility. *Curr Opin Biomed Eng*. 2019;10:69–78.
- Assinck P, Duncan GJ, Hilton BJ, Plemel JR, Tetzlaff W. Cell transplantation therapy for spinal cord injury. *Nat Neurosci*. 2017;20:637–47.
- Liang Y, Zhao X, Hu T, Chen B, Yin Z, Ma PX, Guo B. Adhesive hemostatic conducting injectable composite hydrogels with sustained drug release and photothermal antibacterial activity to promote full-thickness skin regeneration during wound healing. *Small*. 2019;15:1900046.
- Jiao Y, Hafez AM, Cao D, Mukhopadhyay A, Ma Y, Zhu H. Metallic MoS<sub>2</sub> for high performance energy storage and energy conversion. *Small*. 2018;14:1800640.
- Sun G, Yang S, Cai H, Shu Y, Han Q, Wang B, Li Z, Zhou L, Gao Q, Yin Z. Molybdenum disulfide nanoflowers mediated anti-inflammation macrophage modulation for spinal cord injury treatment. *J Colloid Interface Sci*. 2019;549:50–62.
- Comolli N, Donaldson O, Grantier N, Zhukareva V, Tom VJ. Polyvinyl alcohol-polyvinyl pyrrolidone thin films provide local short-term release of anti-inflammatory agents post spinal cord injury. *J Biomed Mater Res, Part B*. 2012;100:1867–73.
- Jiang X, Xiang N, Zhang H, Sun Y, Lin Z, Hou L. Preparation and characterization of poly(vinyl alcohol)/sodium alginate hydrogel with high toughness and electric conductivity. *Carbohydr Polym*. 2018;186:377–83.
- Wang W, Li B, Yang H, Lin Z, Chen L, Li Z, Ge J, Zhang T, Xia H, Li L. Efficient elimination of multidrug-resistant bacteria using copper sulfide nanozymes anchored to graphene oxide nanosheets. *Nano Res*. 2020;13:2156–64.
- Wen N, Jiang B, Wang X, Shang Z, Jiang D, Zhang L, Sun C, Wu Z, Yan H, Liu C. Overview of polyvinyl alcohol nanocomposite hydrogels for electro-skin, actuator, supercapacitor and fuel cell. *Chem Rec*. 2020;20:773–92.
- González-Guisasola C, Ribes-Greus A. Dielectric relaxations and conductivity of cross-linked PVA/SSA/GO composite membranes for fuel cells. *Polym Test*. 2018;67:55–67.
- Alam A, Zhang Y, Kuan H, Lee S, Ma J. Polymer composite hydrogels containing carbon nanomaterials—morphology and mechanical and functional performance. *Prog Polym Sci*. 2018;77:1–18.
- Chen T, Zou H, Wu X, Liu C, Situ B, Zheng L, Yang G. Nanozymatic anti-oxidant system based on MoS<sub>2</sub> nanosheets. *ACS Appl Mater Interfaces*. 2018;10:12453–62.
- Wang L, Gao F, Wang A, Chen X, Li H, Zhang X, Zheng H, Ji R, Li B, Yu X. Defect-rich adhesive molybdenum disulfide/rGO vertical



- heterostructures with enhanced nanozyme activity for smart bacterial killing application. *Adv Mater.* 2020;32:2005423.
20. Lin T, Zhong L, Guo L, Fu F, Chen G. Seeing diabetes: visual detection of glucose based on the intrinsic peroxidase-like activity of MoS<sub>2</sub> nanosheets. *Nanoscale.* 2014;6:11856–62.
  21. Peng J, Weng J. Enhanced peroxidase-like activity of MoS<sub>2</sub>/graphene oxide hybrid with light irradiation for glucose detection. *Biosens Bioelectron.* 2017;89:652–8.
  22. Xu J, Cai R, Zhang Y, Mu X. Molybdenum disulfide-based materials with enzyme-like characteristics for biological applications. *Colloids Surf, B.* 2021;200:111575.
  23. Feicht P, Eigler S. Defects in graphene oxide as structural motifs. *ChemNanoMat.* 2018;4:244–52.
  24. Banerjee A, Arha M, Choudhary S, Ashton RS, Bhatia SR, Schaffer DV, Kane RS. The influence of hydrogel modulus on the proliferation and differentiation of encapsulated neural stem cells. *Biomaterials.* 2009;30:4695–9.
  25. Cai J, Zhang X, Liu W, Huang J, Qiu X. Synthesis of highly conductive hydrogel with high strength and super toughness. *Polymer.* 2020;202:122643.
  26. Nelson NA, Wang X, Cook D, Carey EM, Nimmerjahn A. Imaging spinal cord activity in behaving animals. *Exp Neurol.* 2019;320:112974.
  27. Huang Q, Oya H, Flouty OE, Reddy CG, Howard MA, Gillies GT, Utz M. Comparison of spinal cord stimulation profiles from intra- and extradural electrode arrangements by finite element modelling. *Med Biol Eng Comput.* 2014;52:531–8.
  28. Lee H, Deshmukh S, Wen J, Costa V, Schuder J, Sanchez M, Ichimura A, Pop E, Wang B, Newaz A. Layer-dependent interfacial transport and optoelectrical properties of MoS<sub>2</sub> on ultraflat metals. *ACS Appl Mater Interfaces.* 2019;11:31543–50.
  29. Dou F, Shi L, Song P, Chen G, Juan A, Liu H, Zhang D. Design of orderly carbon coatings for SiO<sub>2</sub> anodes promoted by TiO<sub>2</sub> toward high performance lithium-ion battery. *Chem Eng J.* 2018;338:488–95.
  30. Guiseppi-Elie A. Electroconductive hydrogels: synthesis, characterization and biomedical applications. *Biomaterials.* 2010;31:2701–16.
  31. Vellayappan MV, Balaji A, Subramanian AP, John AA, Jaganathan SK, Murugesan S, Mohandas H, Supriyanto E, Yusof M. Tangible nanocomposites with diverse properties for heart valve application. *Sci Technol Adv Mater.* 2015;16:033504.
  32. Munisso MC, Mahara A, Yamaoka T. Design of in situ porcine closed-circuit system for assessing blood-contacting biomaterials. *J Artif Organs.* 2018;21:317–24.
  33. Park WB, Kim SY, Lee SH, Kim HW, Park JS, Hyun JK. The effect of mesenchymal stem cell transplantation on the recovery of bladder and hindlimb function after spinal cord contusion in rats. *BMC Neurosci.* 2010;11:1–11.
  34. Jelítai M, Schlett K, Varju P, Eisel U, Madarász E. Regulated appearance of NMDA receptor subunits and channel functions during in vitro neuronal differentiation. *J Neurobiol.* 2002;51:54–65.
  35. Zhang T, Gygi SP, Paulo JA. Temporal proteomic profiling of SH-SY5Y differentiation with retinoic acid using FAIMS and real-time searching. *J Proteome Res.* 2020;20:704–14.
  36. Ruschel J, Hellal F, Flynn KC, Dupraz S, Elliott DA, Tedeschi A, Bates M, Sliwinski C, Brook G, Dobrindt K. Systemic administration of epothilone B promotes axon regeneration after spinal cord injury. *Science.* 2015;348:347–52.
  37. Llinás RR. Intrinsic electrical properties of mammalian neurons and CNS function: a historical perspective. *Front Cell Neurosci.* 2014;8:320.
  38. Tripathy SJ, Burton SD, Geramita M, Gerkin RC, Urban NN. Brain-wide analysis of electrophysiological diversity yields novel categorization of mammalian neuron types. *J Neurophysiol.* 2015;113:3474–89.
  39. Kerstein PC, Nichol RH IV, Gomez TM. Mechanochemical regulation of growth cone motility. *Front Cell Neurosci.* 2015;9:244.
  40. Gadani SP, Walsh JT, Smirnov I, Zheng J, Kipnis J. The glia-derived alarmin IL-33 orchestrates the immune response and promotes recovery following CNS injury. *Neuron.* 2015;85:703–9.
  41. Xie X, Mao C, Liu X, Zhang Y, Cui Z, Yang X, Yeung KW, Pan H, Chu PK, Wu S. Synergistic bacteria killing through photodynamic and physical actions of graphene oxide/Ag/collagen coating. *ACS Appl Mater Interfaces.* 2017;9:26417–28.
  42. Hwang J, Bank AM, Mortazavi F, Oakley DH, Frosch MP, Schmähmann JD. Spinal cord  $\alpha$ -synuclein deposition associated with myoclonus in patients with MSA-C. *Neurology.* 2019;93:302–9.
  43. Zeman RJ, Wen X, Ouyang N, Rocchio R, Shih L, Alfieri A, Moorthy C, Etlinger JD. Stereotactic radiosurgery improves locomotor recovery after spinal cord injury in rats. *Neurosurgery.* 2008;63:981–8.

## Publisher's Note

Springer Nature remains neutral with regard to jurisdictional claims in published maps and institutional affiliations.

Ready to submit your research? Choose BMC and benefit from:

- fast, convenient online submission
- thorough peer review by experienced researchers in your field
- rapid publication on acceptance
- support for research data, including large and complex data types
- gold Open Access which fosters wider collaboration and increased citations
- maximum visibility for your research: over 100M website views per year

At BMC, research is always in progress.

Learn more [biomedcentral.com/submissions](https://biomedcentral.com/submissions)

